communications physics

ARTICLE

https://doi.org/10.1038/s42005-023-01304-y OPEN

Mixed orbital states and modulated crystal structures in $La_{1-x}Ca_xMnO_3$ deduced from synchrotron X-ray diffraction

Michael Pissas [1,6]✉, Dimosthenis Stamopoulos[2,6] & Kosmas Prassides [3,4,5,6]✉

In the model manganese perovskites $La_{1-x}Ca_xMnO_3$, several important phenomena have been observed, including ferromagnetic metallic/insulating states, colossal magnetoresistance effects, and charge- and orbital-ordered states. In the past, only compounds with $x = 1/2$, 2/3 and 3/4 and an insulating ground/antiferromagnetic state have been studied. To fully understand the crystal and electronic structures of these materials, it is important to study compounds with doping levels in the range of $0.5 < x < 2/3$. Here we study the crystal structure in a series of compounds with $0.5 < x \leq 0.6$ using ultrahigh-resolution synchrotron X-ray diffraction. The experimental results reveal that all compounds undergo a structural transition at $T < T_{CO}(x) \approx 200 - 220$ K with the concomitant emergence of superlattice Bragg peaks, which can be indexed assuming a superstructure with a modulation propagation vector, τ. At the base temperature of 5 K, the modulation vector of the superstructure $\tau = [\tau_a, 0, 0]$ is parallel to the a-axis, with τ_a varying linearly with x, as $\tau_a \approx 1 - x$. Our results may aid attempts to understand more deeply phenomena related to spin, charge, and orbital ordering, as well as colossal magnetoresistance and symmetry breaking and emergent order in quantum states.

[1] Institute of Nanoscience and Nanotechnology, NCSR Demokritos, Patr. Gregoriou E & 27 Neapoleos Str, 15341 Agia Paraskevi, Athens 15341, Greece. [2] Department of Physics, National and Kapodistrian University of Athens, University Campus, GR-157 84, Athens GR-157 84, Greece. [3] Department of Materials Science, Graduate School of Engineering, Osaka Metropolitan University, Osaka 599-8531, Japan. [4] Advanced Institute for Materials Research (WPI-AIMR), Tohoku University, Sendai 980-8577, Japan. [5] Department of Physics, Graduate School of Science, Osaka Metropolitan University, Osaka 599-8531, Japan. [6] These authors contributed equally: Michael Pissas, Dimosthenis Stamopoulos, Kosmas Prassides. ✉email: m.pissas@inn.demokritos.gr; k.prassides@omu.ac.jp

An important unresolved issue in understanding the physics of $La_{1-x}Ca_xMnO_3$ relates to the physical mechanism responsible for the change in the ground state from ferromagnetic metallic for $0.23 < x < 0.5$ to antiferromagnetic insulating for $0.5 < x \leq 1$ (for reviews see refs. [1,2]). Early and recent studies have explained this dichotomy using the charge and orbital ordering model (CO-OO) adopted, especially when x is equal to a simple fraction, e.g., $x = n/(n+1)$ with $n = 1, 2$, and 3. This model was first proposed in the 1950s by Wollan, Kohler[3] and Goodenough[4] in order to interpret the two distinct sets of magnetic Bragg peaks observed in the $x = \frac{1}{2}$ compound. For $x = \frac{1}{2}$, charge neutrality necessitates an average charge of 3.5 per Mn atom due to the difference in charge between La^{3+} and Ca^{2+}. This charge state can be realized by considering a random distribution of an equal number of Mn^{3+} and Mn^{4+} ions at the lattice points. As the sample is cooled below the so-called charge-ordering temperature (T_{CO}), minimization of the electrostatic energy generates long-range ordering of Mn^{3+} and Mn^{4+} onto specific sites (Fig. 1a). Since Mn^{3+} is a Jahn-Teller–active ion, the e_g orbital degeneracy is lifted, inducing a distortion of the $Mn^{3+}O_6$ octahedra. Minimization of the strain energy induces long-range orbital ordering (essentially strain ordering) concomitant with the charge ordering. In the case of $x = \frac{1}{2}$, it is believed that the elongated Mn^{3+}-O bond is directly related with the $3d_z^2$ orbital, which is oriented along this bond (Fig. 1a).

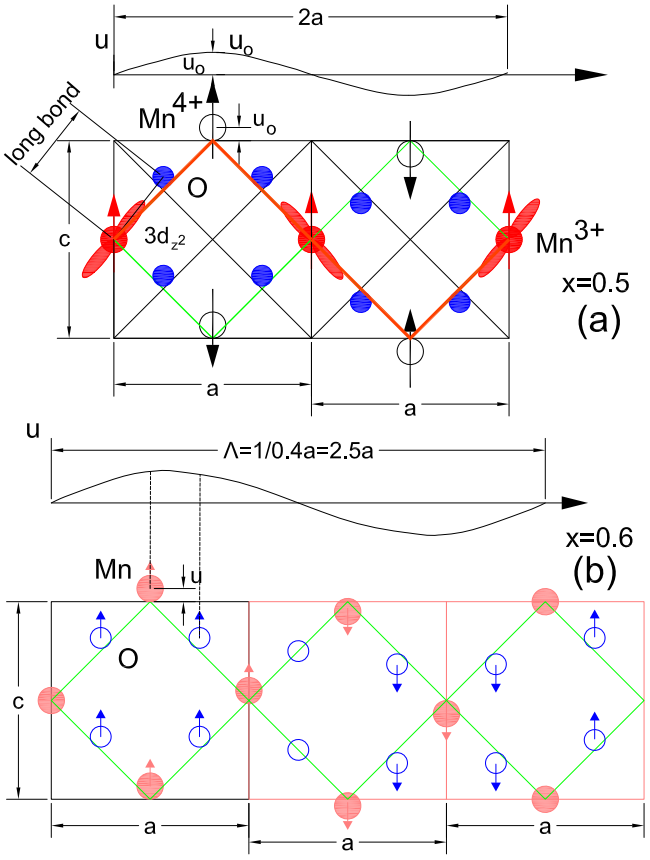

Fig. 1 Schematic projection of the crystal and modulated structures of $La_{1-x}Ca_xMnO_3$ compound. a Schematic projection of the crystal and magnetic structures of $La_{1-x}Ca_xMnO_3$ ($x = 1/2$) along the *b*-axis in the charge and orbital-ordered model. **b** Modulated crystal structure of $La_{1-x}Ca_xMnO_3$ ($x = 0.6$). For clarity, only the Mn and O atoms are shown. $u(r_x)$ represents the displacement of the atoms from average crystal structure positions along the *c*-axis as a function of r_x. Λ is the wavelength of the modulation.

The magnetic structure of $La_{1/2}Ca_{1/2}MnO_3$ includes antiferromagnetic and ferromagnetic interactions. In the *ac*-plane (*Pnmn* description), the magnetic structure can be considered as consisting of ferromagnetic zigzag chains (see Fig. 1a). These chains are coupled antiferromagnetically along the *c*-axis. In a chain (see Fig. 1a), the occupied e_g orbitals of two Mn^{3+} ions are directed toward the intermediate Mn^{4+} ion (where the e_g orbital is unoccupied). Virtual hopping of these e_g-electrons onto empty Mn^{4+}-e_g orbitals produces a ferromagnetic exchange interaction along the chain[2]. Antiferromagnetic interaction between zigzags and along the *b*-axis can be through the antiferromagnetic exchange of the occupied t_{2g}-electrons[2,5]. This model has been widely accepted in the mid-1990s because of the discovery of satellite Bragg peaks in X-ray and transmission electron microscopy (TEM) diffraction data below the charge-ordering temperature (T_{CO})[6–9]. The commensurate wave vector used to index the satellite Bragg peaks when $x = \frac{1}{2}$ can be attributed to a layer-type ABAB ⋯ arrangement of Mn-O layers located perpendicular to the *a*-axis and consisting exclusively of Mn^{3+}(A) and Mn^{4+}(B). Essentially, in this model, Mn^{3+} and Mn^{4+} ions order along the diagonal directions of the Mn-O square lattice of the parent perovskite structure (Fig. 1). The same interpretation is applicable to the compositions with $x = \frac{2}{3}$ and $\frac{3}{4}$, simply by changing the layer sequence to ABBABB ⋯ and ABBBABBB ⋯, respectively. For $x \approx \frac{4}{5}$ and $T < T_{CO}$, the crystal structure becomes monoclinic with two manganese sites without modulation, while the magnetic structure can be described with only one propagation vector, $\mathbf{k}_C = [\frac{1}{2}, 0, \frac{1}{2}]$ (C-structure). The ground state at this particular concentration regime displays only orbital ordering without charge ordering[10,11].

Although this plausible physical picture interprets the majority of the experimental data, especially for the compositions with $x = \frac{1}{2}, \frac{2}{3}$, and $\frac{3}{4}$, there are however some experimental issues which are not compatible with it[12–16]. The most significant problem for the charge-ordered model is that it is not able to predict the commensurate-to-incommensurate modulation observed in the interval $[T_N, T_{CO}]$ for $x = \frac{1}{2}, \frac{2}{3}$, and $\frac{3}{4}$ and the incommensurate superstructure for $\frac{1}{2} < x < \frac{2}{3}$ and $\frac{2}{3} < x < \frac{3}{4}$. Finally, and most importantly, the wave vector, $\boldsymbol{\tau} = (1-x)\mathbf{a}^* = [1-x, 0, 0]$ needed to index the satellite Bragg peaks observed in TEM images by Loudon et al.[16] for $La_{1-x}Ca_xMnO_3$ compositions with $x > 0.5$ is not compatible with the simple charge-ordered arrangement of manganese ions employed for $x = \frac{1}{2}, \frac{2}{3}$, and $\frac{3}{4}$. In addition, it has been demonstrated[16] that the particular variation of the wave vector with x contradicts the interpretation that there exist only four distinct phases (at $x = \frac{1}{2}, \frac{2}{3}, \frac{3}{4}$, and $\frac{4}{5}$) with miscibility gaps at values of x in between[17–19].

In this article, we present a crystallographic study using high-resolution synchrotron X-ray diffraction (SXRD) data in carefully prepared powder $La_{1-x}Ca_xMnO_3$ samples with $0.51 \leq x \leq 0.6$ aiming at the elucidation of the crystal structure below the charge-ordering temperature. In this particular calcium concentration regime, the diffraction patterns at 5 K clearly display satellite Bragg peaks—here, we use a site displacive modulation model and attempt a quantitative analysis of the modulation. First, we present the refinement of the SXRD data based on the average crystal structure and the anisotropic microstrain broadening of the Bragg peaks. Next, modeling of the satellite peaks as function of x and temperature is attempted. The Rietveld refinement results, together with the description of the satellite peaks, show that all the samples in the present study are single-phase materials above and below the charge-ordering temperature. The superstructure arises from a displacive modulation of the average structure with a propagation vector, τ_a, along the *a*-axis varying with x as $\tau_a = 1 - x$. The amplitude of the modulation wave is transverse to the modulation vector, parallel to the *c*-axis.

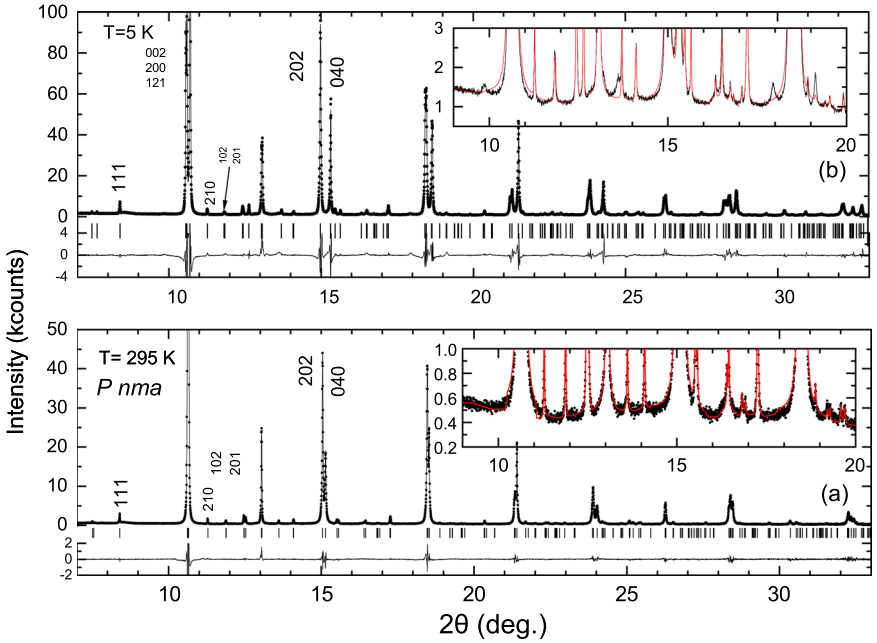

Fig. 2 Rietveld plots of $La_{0.4}Ca_{0.6}MnO_3$ compound based on the average crystal structure. Results of the Rietveld refinement of the average structure (*Pnma* space group) of the $La_{1-x}Ca_xMnO_3$ ($x = 0.6$) composition to synchrotron X-ray powder diffraction data ($\lambda = 0.50008$ Å) at **a** 295 and **b** 5 K. The observed data points are indicated by open circles, while the calculated and difference patterns are shown as solid lines. The positions of the reflections are indicated by vertical lines below the patterns. The insets show enlarged views of a selected area of the profiles near the background level. A number of superlattice peaks present in the measured profile at 5 K (black color) are not accounted for by the average structural model in the calculated profile (red color). These are not present in the measured profile at 295 K.

Results and discussion

Average crystal structure. The average orthorhombic structural model (space group *Pnma*) of the $La_{1-x}Ca_xMnO_3$ compound was successfully used for the refinement of the SXRD patterns of all samples at the studied temperatures. To account for the axial divergence effects and the anisotropic broadening of the Bragg peaks, the profile function #7 and the strain model #3 are used (see Fullprof manual for more details[20]).

The first refinement steps were dedicated to refining the scale factor, the background coefficients, the unit cell parameters, the zero-shift errors, and the full width at half maximum (FWHM) peak profile coefficients, U, V, W, X, and Y. During this procedure, we found that the Gaussian contribution to the peak shape is very small, $U = V = 0$, $W \sim 10^{-4}$(deg.)^2 together with negligible Lorentzian Scherrer size broadening, $Y < 10^{-4}$ deg. both at 295 and 5 K. The peak shape appears to be dominated by the Lorentzian contribution, $X \approx 0.1817$ and 0.1879 deg. at 295 and 5 K, respectively, possibly due to strain fluctuation effects.

Owing to the ultrahigh resolution of the diffractometer, we ascertained that the diffraction peaks are characterized by selective peak broadening, which is closely related to the orbital ordering occurring on cooling below the CO transition ($T < T_{CO}$). This effect is clearly evident when one inspects the $(n, 0, n)$/$(0, 2n, 0)$ family of diffraction lines. Such type of broadening can be phenomenologically reproduced by assuming that the lattice metrics vector, $\boldsymbol{\alpha} = (A, B, C, D, E, F)$, encountered in the expression of the lattice plane spacings, $M_{hkl} = 1/d^2_{hkl} = Ah^2 + Bk^2 + Cl^2 + Dkl + Ehl + Fhk$ is a stochastic vector, which follows a multidimensional Gaussian distribution characterized by the mean value vector and the variance-covariance matrix, $C_{ij} = \mathrm{E}[(\alpha_i - \langle\alpha_i\rangle)(\alpha_j - \langle\alpha_j\rangle)]$ (Stephens' model)[21]. The centroid position of the Bragg peaks is calculated from the average values of the metric parameters, while their broadening from the variance, $\sigma^2(M_{hkl}) = \sum_{i,j} C_{ij}(\partial M/\partial\alpha_i)(\partial M/\partial\alpha_j)$. In an orthorhombic system, the variance of $\sigma^2(M_{hkl})$ can be expressed in terms of six independent parameters[21] (S_{400}, S_{040}, S_{004}, S_{220}, S_{202}, S_{022}) through the relation $\sigma^2(M_{hkl}) = S_{400}h^4 + S_{040}k^4 + S_{004}l^4 + S_{220}h^2k^2 + S_{202}h^2l^2 + S_{022}k^2l^2$, which can be estimated from the results of the Rietveld refinements. In order to simplify the refinements, we kept the isotropic Gaussian U, V, W and Lorentzian X, Y FWHM parameters at zero. Instead, we used the parameter, ξ which 'shares' the anisotropic FWHM in the Gaussian $H_G^2 = (1-\xi)^2D^2\tan^2\theta$ and the Lorentzian $H_L = \xi D\tan\theta$ parts with $D^2 = 10^{-8}8\ln 2(180/\pi)^2\sigma^2(M_{hkl})/M^2_{hkl}$ (see ref. [20] for more details).

The use of Stephens' model led to smoothly proceeding Rietveld refinements of the diffraction data with the reliability factors reduced approximately by a factor of two in comparison to the results of the analysis using isotropic lineshape parameters. A similar methodology was used before in the analysis of the SXRD patterns of the $Bi_{0.15}Ca_{0.85}MnO_3$ manganite measured with the same diffractometer[22]. At the final stages of the refinement, the atomic coordinates and isotropic temperature factors were freely refined. The occupancy factors were kept fixed at the nominal values. After several refinement cycles, we succeeded in achieving very good Rietveld refinement results of the average crystal structure. As an example, the Rietveld plots of the $x = 0.6$ sample at 5 and 295 K are shown in Fig. 2. Tables 1 and 2 summarize the refined structural and microstructural parameters for all samples at 295 and 5 K. For the sample with nominal Ca doping level, $x = 0.51$, the Gaussian distribution of the cell parameters does not reproduce well the experimental Bragg peak shapes in the diffraction profile at $T = 5$ K. In particular, this is especially prominent for the $(2n, 0, 2n)$ and $(0, 4n, 0)$ reflections related to the charge-ordering transition below T_{CO} that appear strongly asymmetric. This results in a very high value of the agreement factor, χ^2. No such issues are evident in the room temperature diffraction data, as can be seen from the low χ^2 value.

Table 1 Refined average crystal-structure parameters at 295 K.

x	0.51	0.53	0.545	0.56	0.57	0.58	0.6
a (Å)	5.4189(1)	5.4148(1)	5.4112(1)	7.4085(1)	5.4060(1)	5.4041(1)	5.3992(1)
b (Å)	7.6365(1)	7.6276(1)	7.6189(2)	7.6096(1)	7.6068(1)	7.6033(1)	7.5925(1)
c (Å)	5.4289(1)	5.4243(1)	5.4209(1)	5.4175(1)	5.4143(1)	5.4122(2)	5.4065(1)
$x_{La/Ca}$	0.0175(1)1	0.0177(1)	0.0176(1)	0.0177(1)	0.0188(1)	0.0180(1)	0.0180(1)
$z_{La/Ca}$	0.0029(1)	0.0027(1)	0.0028(1)	0.003(1)	0.0028(2)	0.0033(2)	0.0026(1)
$B_{La/Ca}$ (Å^2)	1.09(1)	1.49(1)	1.31(1)	1.57(1)	1.76(2)	1.38(2)	1.33(1)
B_{Mn} (Å^2)	0.89(1)	1.36(1)	0.96(1)	1.44(2)	0.3(1)	1.26(2)	1.23(1)
x_{O1}	0.4905(4)	0.4913(5)	0.4910(5)	0.4910(6)	0.4906(6)	0.486(1)	0.4907(5)
z_{O1}	0.9385(5)	0.9364(6)	0.9381(6)	0.9396(8)	0.9391(8)	0.931(1)	0.9385(6)
B_{O1} (Å^2)	1.20(8)	0.97(8)	0.97(8)	1.6(1)	0.33(1)	2.3(1)	0.87(8)
x_{O2}	0.2769(5)	0.2770(6)	0.2778(5)	0.2780(6)	0.2781(7)	0.275(1)	0.2797(6)
y_{O2}	0.0314(2)	0.0313(3)	0.0312(3)	0.0315(3)	0.0307(4)	0.034(4)	0.0313(3)
z_{O2}	0.2752(5)	0.2768(6)	0.2748(6)	0.2756(7)	0.2755(8)	0.274(1)	0.2766(6)
B_{O2} (Å^2)	1.09(5)	1.34(5)	1.04(5)	1.40(6)	0.49(6)	0.9(1)	1.21(5)
S_{400}	0.105(1)	0.081(2)	0.213(4)	0.086(2)	0.131(1)	0.203(6)	0.170(3)
S_{040}	0.0717(1)	0.072(2)	0.161(2)	0.112(1)	0.114(1)	0.125(2)	0.120(1)
S_{004}	0.133(1)	0.127(2)	0.213(4)	0.162(3)	0.170(3)	0.266(6)	0.170(2)
S_{220}	0.005(3)	0.022(3)	−0.017(5)	0.045(6)	−0.033(6)	−0.10(1)	−0.083(3)
S_{202}	0.534(6)	0.510(7)	1.16(2)	0.76(1)	0.73(1)	0.47(1)	0.93(1)
S_{022}	−0.009(3)	−0.034(4)	−0.017(5)	0.007(7)	−0.043(7)	−0.20(1)	−0.083(3)
ξ	1.0	1.0	1.0	1.0	1.0	1.0	1.0
Mn-O1 × 2 (Å)	1.9384(5)	1.9384(6)	1.9346(6)	1.9309(7)	1.9346(6)	1.938(1)	1.930(5)
Mn-O2 × 2 (Å)	1.937(3)	1.941(3)	1.929(3)	1.931(4)	1.929(3)	1.936(6)	1.95(2)
Mn-O2 × 2 (Å)	1.959(3)	1.943(3)	1.951(3)	1.948(4)	1.951(3)	1.943(6)	1.96(3)
R_p (%)	5.1	7.6	4.9	5.3	6.4	8.4	5.0
R_{wp} (%)	5.9	8.4	6.4	7.3	8.3	11.2	6.0
χ^2 (%)	4.75	3.4	4.2	4.6	12.1	10.7	3.3
R_B (%)	2.0	2.4	2.1	2.5	6.0	6.9	2.0

Refined average crystal-structure parameters from synchrotron X-ray powder diffraction patterns of $La_{1-x}Ca_xMnO_3$ ($x = 0.51$, 0.53. 0.545, 0.56, 0.57, 0.58, 0.60) based on the *Pnma* (No. 62) space group at $T = 295$ K ($\lambda = 0.50008$ Å). The La, Ca and apical oxygen (O1) atoms occupy the 4*c* ($x, \frac{1}{4}, z$) site, the Mn atoms the 4*b* ($0, 0, \frac{1}{2}$) site, and the equatorial oxygen (O2) atoms the general 8*d*(x, y, z) site. The site occupancies were kept fixed during refinement at values consistent with the nominal stoichiometry. Numbers in parentheses are statistical errors at the last significant digit. The units of Stephens parameters, S_{HKL}, are (10^{-8}Å^{-4}) (Fullprof implementation).

Figure 3 shows the variation of the lattice parameters at $T = 5$ K with increasing Ca^{2+} concentration, x. The reduction of all lattice parameters with increasing x can be accounted for by the smaller ionic radius of Ca^{2+} than that of La^{3+}. Here we point out that the monotonic variation of the lattice parameters with x at 5 K (as well as at 295 K) indicates that the average calcium concentration varies from sample to sample in a controlled way.

Analysis of the satellite peaks. Having successfully described the SXRD patterns with the *Pnma* space group structural model for all samples, a careful inspection of the profile near the background level (inset of Fig. 2b) revealed several weak peaks not predicted by the average-structure model. These peaks can be indexed using fractional Miller indices. Equivalently, they can be reproduced with a modulation wave vector, $\boldsymbol{\tau}_s = [\tau_a, 0, 0]$ with $\tau_a = 1 - x$. They are all satellites of the strongest Bragg peaks originating from the aristotype cubic perovskite structure. In all cases, La/Ca and Mn contribute constructively to the structure factor, while the Miller index, ℓ is non-zero [e.g., $(1 \pm \tau_a, 2, 1)$, $(\tau_a, 0, 2)$ (unresolved) $(\tau_a, 2, 2)$, $(2 \pm \tau_a, 0, 2)$, $(1 \pm \tau_a, 2, 3)$] with the satellite-peak intensity increasing as ℓ increases.

These observations can be nicely explained by (Eq. 7, in Supplementary Note 1) because the most intense first-order satellites are expected to be connected with fundamental Bragg peaks of the highest structure factors (e.g., the peaks deriving from the cubic perovskite structure (1, 2, 1), (2, 0, 2), and (1, 2, 3) reflections) and the highest ℓ index. This is observable up to a certain Bragg angle where the reduction of the atomic scattering factors is not overcome by the increase in ℓ. Recalling that the structure factor of the satellite peaks is $\sim \mathbf{u}_i^0 \cdot (\mathbf{Q} - \boldsymbol{\tau})$ (see Supplementary Note 1), we can conclude that the polarization of the modulation is along the *c*-axis. Similar satellite peaks but with *a*-components of the structural modulation vector equal to $\frac{1}{2}$, $\frac{1}{3}$, and $\frac{1}{4}$ were observed in $La_{1-x}Ca_xMnO_3$ with $x = \frac{1}{2}$, $x = \frac{2}{3}$, and $x = \frac{3}{4}$, respectively[6–8] and provided the diffraction signatures of the so-called 2*a*, 3*a*, and 4*a* superstructures. In order to analyze the structural modulation quantitatively, we simulated the SXRD patterns using the atomic displacement model described in Supplementary Note 1 (Eq. 4, Supplementary Note 1), assuming that below T_{CO}, the crystal structure is harmonically modulated. It was immediately apparent that second- and higher-order satellites made negligible contributions to the calculated patterns. Consequently, for simplicity, we consider only first-order satellites. The zeroth-order, $m = 0$ Bragg peaks (Eq. 6, in Supplementary Note 1) are reproduced by the refined average-structure and microstructure model described earlier. A simple inspection of the satellite Bragg peaks also revealed that they had larger linewidths than those of the zeroth-order ones. We accounted for this broadening by employing as a profile function a Lorentzian curve with a FWHM varying by a Scherrer-type equation, $\Delta 2\theta \sim L/\cos\theta$. Figure 4 shows the experimental and calculated SXRD patterns of the samples $La_{1-x}Ca_xMnO_3$ ($0.5 < x \leq 0.6$) at 5 K.

The following conclusions were reached after performing a series of trial-and-error simulations by varying the amplitude and the phase of the modulation for each atom. (1) The very good data statistics show that *only* first harmonics are observed, implying that the structural modulation in $La_{1-x}Ca_xMnO_3$

Table 2 Refined average crystal-structure parameters at 5 K.

x	0.51	0.53	0.545	0.56	0.57	0.58	0.6
a (Å)	5.4405(1)	5.4362(1)	5.4316(1)	5.4274(1)	5.4248(1)	5.4213(1)	5.4149(1)
b (Å)	7.5261(1)	7.5171(1)	7.5131(1)	7.5099(1)	7.5078(1)	7.5053(1)	7.5030(1)
c (Å)	5.4665(1)	5.4596(1)	5.4531(1)	5.4477(1)	5.4441(1)	5.4398(1)	5.4315(1)
$x_{La/Ca}$	0.0163(2)	0.0178(1)	0.0180(1)	0.0183(1)	0.0185(1)	0.0188(1)	0.0186(2)
$z_{La/Ca}$	0.0028(3)	0.0030(1)	0.0030(1)	0.0030(1)	0.0029(1)	0.0036(2)	0.0035(2)
$B_{La/Ca}$ (Å^2)	0.72(2)	0.87(1)	0.88(9)	0.85(1)	1.13(1)	1.21(2)	0.97(1)
B_{Mn} (Å^2)	0.67(3)	0.90(2)	0.87(1)	0.92(1)	1.04(1)	1.24(2)	0.85(2)
x_{O1}	0.481(1)	0.4857(7)	0.4851(6)	0.4846(7)	0.4866(6)	0.4861(9)	0.4860(8)
z_{O1}	0.932(1)	0.9312(6)	0.9325(6)	0.9344(7)	0.9341(6)	0.9324(8)	0.9341(7)
B_{O1} (Å^2)	0.5(1)	0.85(8)	0.80(7)	0.63(9)	1.01(8)	2.3(1)	0.6(1)
x_{O2}	0.272(1)	0.2723(7)	0.2727(6)	0.2737(6)	0.2742(6)	0.2702(9)	0.2754(8)
y_{O2}	0.032(6)	0.0330(3)	0.0320(2)	0.0324(3)	0.0323(3)	0.0398(4)	0.0331(3)
z_{O2}	0.271(1)	0.2729(7)	0.2728(6)	0.2753(7)	0.2748(6)	0.2715(9)	0.2759(7)
B_{O2} (Å^2)	0.8(1)	0.91(6)	0.92(5)	0.76(6)	0.84(5)	1.32(7)	0.74(7)
S_{400}	0.31(1)	0.242(4)	0.252(4)	0.298(5)	0.251(1)	0.246(5)	0.257(5)
S_{040}	0.232(5)	0.058(1)	0.060(1)	0.063(1)	0.055(1)	0.059(1)	0.066(1)
S_{004}	0.46(1)	0.323(4)	0.331(4)	0.402(6)	0.325(4)	0.332(6)	0.328(6)
S_{220}	−0.14(2)	0.070(6)	0.081(6)	0.105(9)	0.085(6)	0.051(9)	0.052(9)
S_{202}	0.87(3)	0.56(1)	0.66(1)	0.83(2)	0.74(1)	0.71(2)	0.81(2)
S_{022}	−0.16(1)	0.085(7)	0.102(7)	0.130(9)	0.109(7)	0.075(9)	0.103(9)
ξ	1.0	1.0	1.0	1.0	1.0	1.0	1.0
Mn-O1 × 2 (Å)	1.920(1)	1.9179(5)	1.9156(6)	1.9128(7)	1.9122(6)	1.9134(1)	1.9110(7)
Mn-O2 × 2 (Å)	1.946(8)	1.947(4)	1.948(3)	1.954(4)	1.949(3)	1.956(5)	1.946(4)
Mn-O2 × 2 (Å)	1.956(8)	1.953(4)	1.946(4)	1.940(4)	1.943(4)	1.944(5)	1.941(4)
R_p (%)	11	7.4	7.1	8.0	7.1	8.9	6.6
R_{wp} (%)	16	11.3	10.8	12.1	10.2	12.2	9.7
χ^2 (%)	167	16.3	18.4	28.3	13.4	14.7	23.5
R_B (%)	6.3	5.3	3.9	4.2	4.1	7.2	3.07

Refined average crystal-structure parameters from synchrotron X-ray powder diffraction patterns of $La_{1-x}Ca_xMnO_3$ ($x = 0.51$, 0.53. 0.545, 0.56, 0.57, 0.58, 0.60) based on the *Pnma* (No. 62) space group at $T = 5$ K ($\lambda = 0.50008$ Å). The La, Ca and apical oxygen (O1) atoms occupy the 4*c* ($x, \frac{1}{4}, z$) site, the Mn atoms the 4*b* ($0, 0, \frac{1}{2}$) site, and the equatorial oxygen (O2) atoms the general 8*d*(x, y, z) site. The site occupancies were kept fixed during refinement at values consistent with the nominal stoichiometry. Numbers in parentheses are statistical errors at the last significant digit. The units of Stephens parameters, S_{HKL}, are (10^{-8}Å^{-4}) (Fullprof implementation).

($x \geq 0.5$) is harmonic, with a single modulation vector. (2) The modulation vector, $\boldsymbol{\tau} \approx (1-x)\boldsymbol{a}^*$, is along the *a*-axis and varies continuously with *x*. (3) The polarization of the modulation is parallel to the *c*-axis ($\boldsymbol{u}_i^0 \parallel c$-axis, see Fig. 1b). (4) The displacements of all atoms are in-phase. (5) The best agreement between observed and calculated patterns is obtained when the modulation amplitudes of (La,Ca), (Mn, O1), and O2 atoms are ≈0.016, ≈0.012, and ≈0.016 fractional units, respectively (e.g., for (La,Ca) the amplitude is estimated to be $u = 0.016c \approx 0.09$ Å). (6) Finally, the effective size of the diffraction domains contributing to the satellite peaks is estimated to be about 200–300 Å for all samples at 5 K. Here, we also note that one cannot exclude a small *c*-component of the wave modulation vector $[\tau_a, 0, \tau_c \approx 0.003]$ in accounting for the extra broadening of the satellite Bragg peaks. In TEM studies, such an extra component has been attributed[23,24] to anti-phase domains.

Figure 5 shows the concentration dependence of the *a*-component, τ_a of the modulation vector deduced from the location of the satellite peaks in the SXRD patterns. Although the experimental points slightly deviate from the $\tau_a = 1 - x$ line, it appears reasonable to deduce a linear variation in the ideal case. The deviation of the observed points from the ideal curve could be attributed to a systematic error in the value of real calcium concentration (i.e., there may be a small constant error in *x* when compared with the nominal values). The obtained results are in good agreement with the data of Loudon et al.[16].

Results of variable temperature diffraction data. Let us continue by next examining the temperature variation of the SXRD patterns. Figure 6 depicts the temperature variation of the unit cell parameters for samples with $x = 0.53$, 0.57, and 0.6. The lattice

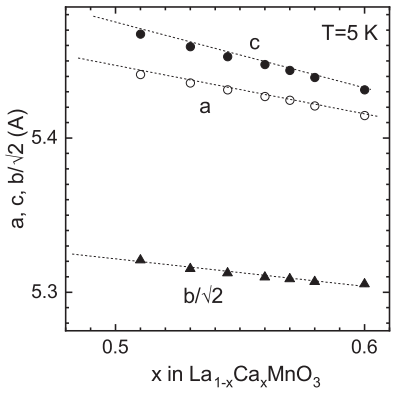

Fig. 3 Unit cell constants of the average crystal structure of $La_{1-x}Ca_xMnO_3$ ($0.5 < x \leq 0.6$) at 5 K. Variation of the unit cell constants of $La_{1-x}Ca_xMnO_3$ ($0.5 \leq x \leq 0.6$) with changing *x* at 5 K. Error bars are smaller than the data points.

metrics respond sensitively to temperature on cooling, with *a* and *c* increasing abruptly and $b/\sqrt{2}$ undergoing a step-like decrease. The temperature range at which the changes occur depends on the Ca concentration, *x*. This variation corresponds to a structural transition, which has been attributed for $x = \frac{1}{2}$, $x = \frac{2}{3}$, and $x = \frac{3}{4}$ to the so-called charge-ordering transition at temperatures, T_{CO}. We would like to point out that the terms "charge-ordering temperature" or "charge-ordering transition" are used here to denote the temperature where the zero-field-cooled magnetization curves show a local maximum, the average crystal-structure lattice parameters change abruptly, and satellite Bragg peaks are

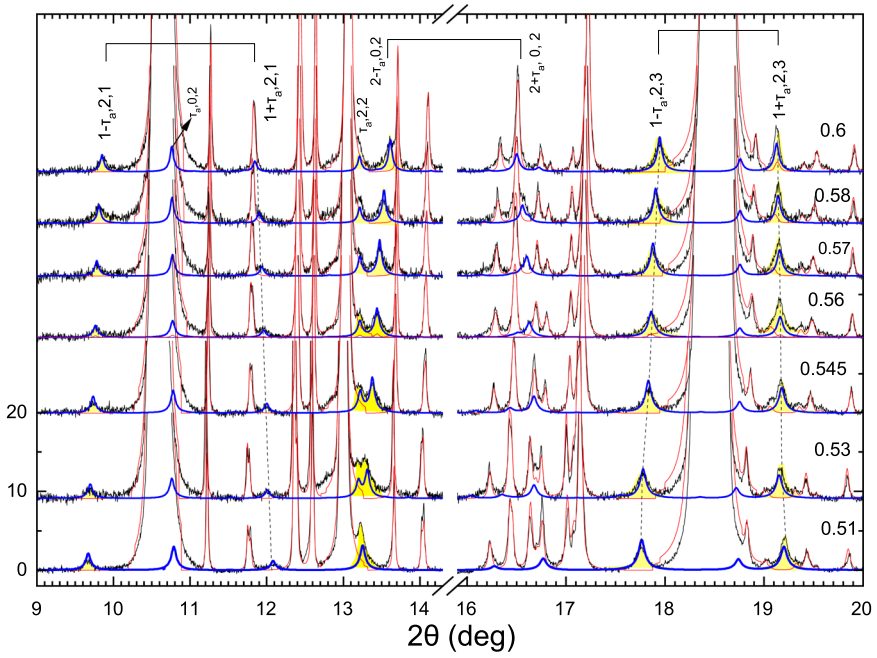

Fig. 4 Experimental and simulated X-ray diffraction patterns of the $La_{1-x}Ca_xMnO_3$ ($0.5 < x \leq 0.6$) compositions at 5 K. The black, red, and blue lines correspond to the experimental, to the calculated using the average crystal structure model, and to the calculated using the first-order satellites model, respectively. The well-resolved superlattice peaks are highlighted in yellow. Superlattice peaks with appreciable intensity have $k = 2n$.

observed both in TEM and SXRD measurements. This transition does not necessarily mean ordering of the electric charges.

We define the transition temperature as the temperature at which the $db(T)/dT$ curves show a maximum, as indicated by arrows in Fig. 6. This coincides with the temperature at which a peak is observed in the bulk magnetization data[25,26]. The changes observed in the temperature variation of the unit cell parameters at T_{CO} are accompanied by the appearance of the satellite Bragg peaks, a fact signaling that two distortion mechanisms start to operate simultaneously. The first is related to the ordering of the deformation of the Mn-O_6 octahedral units and the second with the development of the superstructure. The changes in the unit cell parameters at T_{CO} correlate with the shortening of the Mn-O1 apical bond length to ~1.91 Å, compared with the value of ~1.93 Å at $T > T_{CO}$. This bond is roughly parallel to the b-axis, and consequently, its decrease is directly related to the temperature variation of the b-axis. At the same time, the in-plane Mn-O2 bonds increase slightly for $T < T_{CO}$. It is interesting to note that the magnitude of these changes is much smaller than the amplitude of the ion displacements of ≈0.09 Å. Based on the correlation of the Mn-O_6 octahedral deformations with the Jahn-Teller effect, the average distortion is of the apically compressed type, implying that the d_z^2 orbital lies in the a–c plane. Therefore, in the structural transition occurring at $T < T_{CO}$, the d_z^2 orbitals are brought into the a–c plane, while the harmonic modulation with amplitude along the c-axis may be related to the charge localization.

Panels (a1, b1, c1) of Fig. 7 depict the temperature evolution of selected areas of the SXRD patterns in which satellite peaks $(1 \pm \tau_a, 2, 3)$ with maximal intensity are present for samples with $x = 0.53, 0.57$, and 0.6, respectively. The $(1 - \tau_a, 2, 3)$ Bragg peak is displaced toward higher angles on heating, whereas the $(1 + \tau_a, 2, 3)$ to lower angles, implying that τ_a is temperature dependent. The satellite peaks eventually disappear above T_{CO}. Given their weak intensity, it is difficult to conclude with certainty whether the satellites disappear suddenly or gradually, a fact related to the character of the phase transition. By invoking the

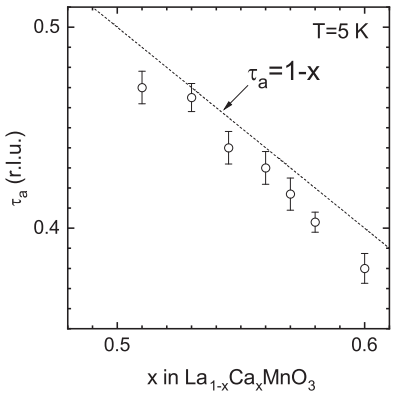

Fig. 5 Concentration variation of *a*-component of the modulation vector at 5 K. Variation of the a-component, τ_a of the modulation vector with concentration, x in $La_{1-x}Ca_xMnO_3$ at 5 K.

information from the magnetic measurements, the disappearance of the satellites is most likely sudden, corresponding to a first-order transition.

Panels (a2, b2, c2) of Fig. 7 show the temperature variation of the non-zero a-component of the modulation vector, τ_a, together with that of the integrated intensity of the $(1 - \tau_a, 2, 3)$ satellite Bragg peak. Within standard deviation, for $T < T_N$, $\tau_a(T)$ is temperature independent, while for $T > T_N$, τ_a decreases markedly with temperature, meaning that the wavelength of the modulation becomes larger. This particular temperature dependence of τ_a agrees well with the predictions of Milward, Calderon, and Littlewood (see Fig. 1b of ref. [27]).

Figure 8 shows the temperature dependence of the S_{HKL} parameters for the $x = 0.57$ sample. Similar results are obtained for all the other samples. The temperature variation of the S_{HKL} parameters changes drastically at charge-ordering temperature. The largest values of the variance of the unit cell parameters, especially for the b-axis, are observed at T_{CO}. The unusual Bragg

peak broadening essentially originates from the peak in the standard deviation of the b parameter (Fig. 8) at T_{CO}, which in turn is related to the orbital ordering of the d_z^2 orbital in the a–c plane. It is tempting to associate the observed selective peak broadening with the remarkable softening of the shear modulus observed[28] on approaching the charge-ordering temperature, T_{CO}. As the shear modulus reaches its minimum value, the crystal structure becomes unstable to strains, and it changes to a more distorted, lower-symmetry structure.

This type of anisotropic peak broadening is observable because of the ultrahigh resolution of the present diffractometer, and it is inherent in the structural phase transition at T_{CO} in the polycrystalline samples. All studied samples display single-phase X-ray diffraction patterns (absence of macroscopic phase segregation) both above T_{CO} and at 5 K. Clear phase separation (in the sense of multiple diffraction pattern contributions) has been observed in $La_{0.25}Ca_{0.75}MnO_3$[8] and $Bi_{0.15}Ca_{0.85}MnO_3$[22] samples, measured with the same diffractometer.

It is also interesting to note that although the SXRD pattern of the sample with $x = 0.6$ at 5 K can be reproduced here with a single modulated phase, the neutron diffraction pattern at 5 K contains magnetic Bragg peaks[26], related to the $x = 1/2$ and 2/3 phases. This is an unusual result implying that either the magnetic structure originates from a single phase consisting of three Fourier components, or the phase separation cannot be resolved in the SXRD patterns.

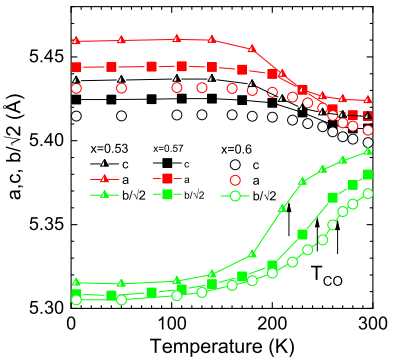

Fig. 6 Temperature variation of the unit cell parameters of $La_{1-x}Ca_xMnO_3$ compound with $x = 0.53$, 0.57, and 0.6. The arrows denote the charge-ordering transitions located at the temperatures where the slope of each $b(T)$ curve is at a maximum. Error bars are smaller than the data points (the standard deviations have been calculated by fullprof program as described in the fullprof manual page 43).

Comparison with other studies. Experimental and theoretical studies to date have proposed that the so-called charge-ordered state (or stripe phase) in the $La_{1-x}Ca_xMnO_3$ ($0.5 \le x \le 0.75$) series may be related to the formation of charge density waves (CDW)[16,27,29–34]—namely, lattice-distortion waves and their associated conduction-electron density waves, accompanied by the opening of a gap in the one-electron excitation spectrum at the Fermi level[35,36]. The idea of a CDW wave has its origin in Peierls[37,38], who proved that an ideal one-dimensional crystal with a partially occupied conduction band is unstable to the formation of a CDW state at low temperatures.

The CDW scenario, as appropriately modified for manganites[27], reproduces some of the aspects of the experimental data of the $La_{1-x}Ca_xMnO_3$ ($x > 0.5$) compounds. However, there are two key issues needing more detailed experimental verification in order to reach a final resolution of this fundamental issue. (1) Above the Peierls transition, T_p ($T_p \equiv T_{CO}$), the compounds are insulators (the resistivity has an activated temperature dependence), not conductors. Cox et al.[33] have explained this issue by invoking the role of large impurity density to account for the insulating behavior well above T_{CO}. (2) The Peierls transition is energetically favorable only for materials with a quasi-one-dimensional band structure or with certain Fermi surface topologies with parallel parts of the Fermi surface connected by a reciprocal lattice vector (i.e., nesting)[39].

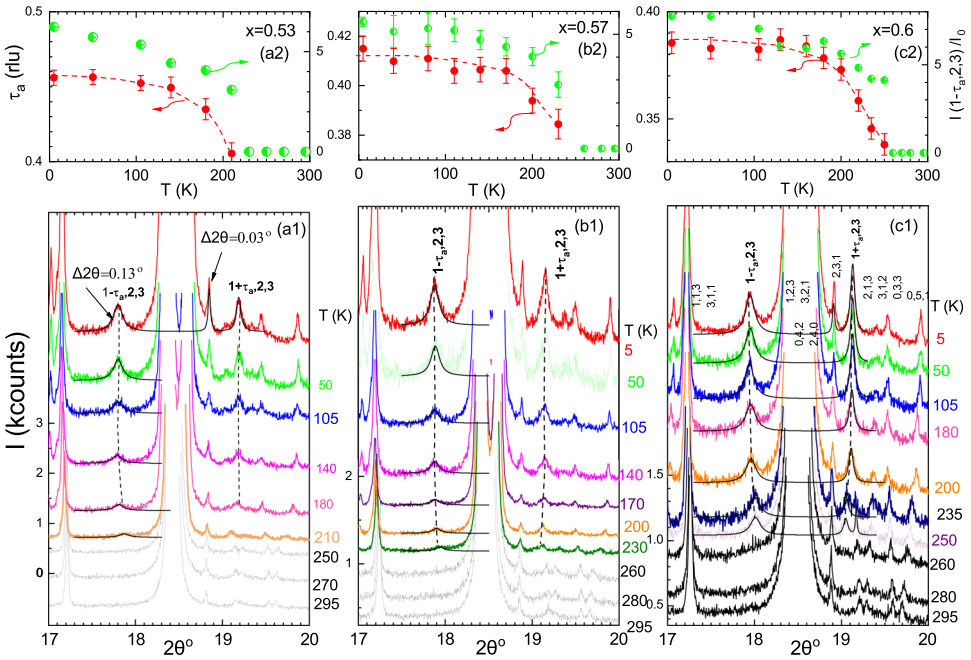

Fig. 7 Satellite Bragg peaks for the samples with $x = 0.53$, 0.57, and 0.6. a1, **b1**, **c1** Selected regions of the synchrotron X-ray powder diffraction patterns showing the temperature evolution of the satellite Bragg peaks with Miller indices $(1 \pm \tau_a, 2, 3)$ for the $x = 0.53$, 0.57, and 0.6 samples. **a2**, **b2**, **c2** Temperature variation of the a-component of the modulation wave vector (left axis) and of the normalized integrated intensity of the $(1 - \tau_a, 2, 3)$ satellite Bragg peak (right axis) for each composition. The dashed and continuous lines through the $\tau_a(T)$ and $I(1 - \tau_a, 2, 3)/I_0$ points are guides to the eye.

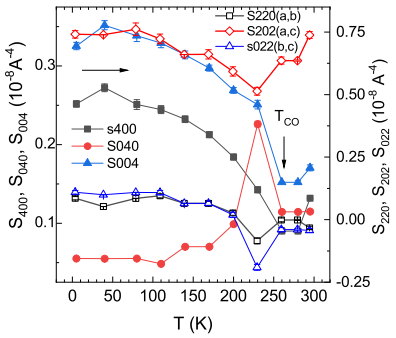

Fig. 8 Temperature variation of the variance and covariance coefficients. Temperature variation of the variance and covariance coefficients of the unit lattice parameters of the $La_{1-x}Ca_xMnO_3$, $x = 0.57$ composition. Error bars are smaller than in some data points (the standard deviations have been calculated by fullprof program as described in the fullprof manual page 43).

Obviously, these issues need to be addressed by a clear theoretical and experimental study.

It is interesting to refer here to the conclusions[40–43] from THz spectroscopy studies in manganites samples with similar calcium ($x > 0.5$) concentration as CDWs are expected to give low-energy excitations in the THz frequency range. Frequency-domain THz spectroscopic data[41] in a sample with $x = 3/4$ and for samples[40] with $0.5 \le x \le 1$ do not show any feature that can be connected with a collective response (charge density wave) of the spatially charge-ordered state. Instead, the observed THz resonances have been interpreted by Goshunov et al.[40] and Shukova et al.[41] as "acoustical lattice vibrations that acquire optical activity when the Brillouin zone is folded due to the superstructure in the CO state".

Neutron diffraction measurements[25,26] of some older as well as the same samples used in the present work revealed that the samples with $1/2 < x \le 0.56$ display magnetic Bragg peaks similar to those observed for $x = \frac{1}{2}$, the so-called charge exchange (CE) magnetic structure. The CE magnetic Bragg peaks for $x = \frac{1}{2}$ have been successfully interpreted by a layer-type ordering of Mn^{3+} and Mn^{4+} ions (stacked along the a-axis), forming ferromagnetic zigzag chains coupled antiferromagnetically. The two families of magnetic Bragg peaks have been directly connected with the two charge states. Specifically, the propagation vector, $\mathbf{k}_C = [\frac{1}{2}, 0, \frac{1}{2}]$ has been attributed to "Mn^{4+}"-like ions, while the $\mathbf{k}_E = [0, 0, \frac{1}{2}]$ one (see ref. [6]) to "Mn^{3+}"-like ions. When we tried to apply this model to the samples with $1/2 < x \le 0.56$, we discovered several key features, which put in doubt the validity of the classical Goodenough CE model when $x > 0.5$ in agreement with the present SXRD data. The most spectacular observation is that the calculated E-type $(1, 1, \frac{1}{2})$ magnetic Bragg peaks are located at slightly higher angles in comparison to the experimental ones. In addition, the same peaks display a pronounced broadening. These experimental findings advocate that the simple CE model is inappropriate for compositions with Ca concentrations, $1/2 < x \le 0.56$. In order to index the E-type magnetic peaks, we have to use an incommensurate propagation vector, $\mathbf{k}_E = [\varepsilon_E, 0, 1/2]$, instead of the commensurate one, $\mathbf{k}_E = [0, 0, 1/2]$ used for $x = 1/2$. The incommensurate component, ε_E, is directly connected with the a-component of the structural modulation vector through the relationship, $\varepsilon_E = 1/2 - \tau_a$.

Since the difference of the charge between the Mn sites is not so large to produce measurable scattering intensity, the satellite intensities in the SXRD patterns arise mainly from the displacement of the cations and the coordinated oxygen atoms. One may speculate that the modulation is related to a mixed-orbital state of the Mn e_g levels. Such an orbital state could be related to the mixed-orbital state, $[\cos(\theta/2)d_{3z^2-r^2} - \sin(\theta/2)d_{x^2-y^2}, \sin(\theta/2)d_{3z^2-r^2} + \cos(\theta/2)d_{x^2-y^2}]$ proposed by Tao and co-workers[44]. The mixing angle, θ, changes continuously along the a-axis leading to a transverse displacive modulation with the $\tau_a(x)$ wave number changing continuously with x. At the $x = 1/2$, 2/3, and 3/4 compositions, the modulation becomes commensurate, and therefore, it can be interpreted with the classical Goodenough charge and orbital model.

The temperature dependence of the modulation vector, $[\tau_a(x, T), 0, 0]$, can be attributed to phase defects of the displacement field, $\mathbf{u}(\mathbf{x}) = \mathbf{u}_0(\mathbf{x})\exp[i\boldsymbol{\tau}\cdot\mathbf{r} + \phi(\mathbf{r})]$. The average value of the random jumps of the phase can be effectively described by a phase gradient, $\langle\phi(\mathbf{x})\rangle = \Delta\boldsymbol{\tau}\cdot\mathbf{x}$, which leads to a change in the modulation vector, $\boldsymbol{\tau}' = \boldsymbol{\tau} + \Delta\boldsymbol{\tau}$. This model has been proposed by Baggari et al.[45,46] in order to interpret the evolution of scanning transmission electron contrasts measured in a $\boldsymbol{\tau} = [1/3, 0, 0]$ $Bi_{1-x}Sr_{x-y}Ca_yMnO_3$ ($x = 0.65$, $y = 0.47$) compound. This phase inhomogeneity is absent at low temperatures and spreads in the sample as the charge-ordering temperature is approached. A similar explanation for the temperature dependence of $\tau_a(x, T)$ below and near the charge-ordering temperature has been proposed by Tao and co-workers[44,47]. The temperature change of $\tau_a(x, T)$ has been attributed to defects (dislocations) of the electronic superstructure mainly arising from orbital degrees of freedom, not necessarily connected with the crystal-structure defects. Finally, we note that the observed structural incommensurability may be related to the short-range structure, comprising a superposition of charge-disordered $Mn^{3.5+}$ and orbital-ordered Mn^{3+} layers, recently proposed by Chen et al.[48].

Conclusions

Thanks to the ultrahigh resolution of the synchrotron X-ray diffraction data, we have established that all studied $La_{1-x}Ca_xMnO_3$ ($x = 0.51$, 0.53, 0.545, 0.56, 0.57, 0.58, and 0.6) compositions are single phase in the entire temperature range of the present work (from room temperature down to 5 K). At the same time, all samples adopt a modulated crystal structure at temperatures $T < T_{CO}$. The modulated structure can be modeled by an atomic displacement model, which incorporates a harmonic modulation, $\mathbf{u}_j(\mathbf{R}) = \mathbf{u}_j^0\cos[2\pi\boldsymbol{\tau}\cdot(\mathbf{R} + \mathbf{r}_i) + \phi_i]$ with a modulation wave vector, which obeys roughly the empirical relation, $\boldsymbol{\tau} = (1 - x)\boldsymbol{a}^*$, and with polarization along the c-axis. The observed temperature variation of $\boldsymbol{\tau}$ may be related to phase defects of the order parameter that describes the lattice displacements, arising either from charge or orbital ordering. Our results here on the model $La_{1-x}Ca_xMnO_3$ manganite phases may aid attempts at a deeper understanding of the currently debated condensed matter physics topics regarding spin, charge, and orbital ordering, as well as symmetry breaking and emergent order in quantum states.

Methods

Samples with nominal stoichiometry $La_{1-x}Ca_xMnO_3$ ($x = 0.51$, 0.53. 0.545, 0.56, 0.57, 0.58, and 0.60) were synthesized by thoroughly mixing high-purity stoichiometric amounts of $CaCO_3$, La_2O_3, and MnO_2. The mixed powders were reacted in air at temperatures up to 1400 °C for several days with intermediate grindings. In the final reaction step, the samples were cooled slowly to 25 °C. High-resolution SXRD powder diffraction patterns were measured with the multi-detector powder diffractometer on the ID31 beamline (now ID22) at the ESRF (Grenoble, France). Powder samples were sealed in thin-wall borosilicate glass capillaries ($d = 0.5$ mm), inserted in a continuous-flow cryostat and rotated during data collection. Data were collected in Debye-Scherrer (transmission) configuration with $\lambda = 0.50008$ Å. Next, they were rebinned to a 0.002° step in the range of 4–60°. Average crystal-structure models were refined to the SXRD data using the Rietveld

method with the FULLPROF suite of programs[20]. In order to analyze the superlattice peaks qualitatively, we consider that the average *Pnma* crystal structure is harmonically modulated. Simulations of the SXRD patterns are made by a purpose-written FORTRAN program, taking into account only first-order satellites. Based on this program, we estimated the modulation wave vector as a function of calcium concentration and temperature. In addition, based on the best agreement between theoretical and experimental satellite-peak intensities, we also estimated the polarization and the amplitude of the modulation vector for each atom.

Data availability

All relevant data are available from the authors (M.P.) upon request.

Received: 26 January 2023; Accepted: 11 July 2023;
Published online: 26 July 2023

References

1. Markovich, V., Wisniewski, A. & Szymczak, H. Magnetic properties of perovskite manganites and their modifications. *Handbook of Magnetic Materials*, Vol. 22 (Elsevier, 2014).
2. Khomskii, D. I. *Transition Metal Compounds* (Cambridge University Press, 2014).
3. Wollan, E. O. & Koehler, W. C. Neutron diffraction study of the magnetic properties of the series of perovskite-type compounds $[(1-x)\mathrm{La}, x\mathrm{Ca}]\mathrm{MnO_3}$. *Phys. Rev.* **100**, 545–563 (1955).
4. Goodenough, J. B. Theory of the role of covalence in the perovskite-type manganites $[\mathrm{La}, \mathrm{M(II)}]\mathrm{MnO_3}$. *Phys. Rev.* **100**, 564–573 (1955).
5. Goodenough, J. B. *Magnetism and the Chemical Bond* (Wiley, 1963).
6. Radaelli, P. G., Cox, D. E., Marezio, M. & Cheong, S.-W. Charge, orbital, and magnetic ordering in $\mathrm{La_{0.5}Ca_{0.5}MnO_3}$. *Phys. Rev. B* **55**, 3015–3023 (1997).
7. Radaelli, P. G., Cox, D. E., Capogna, L., Cheong, S.-W. & Marezio, M. Wigner-crystal and bi-stripe models for the magnetic and crystallographic superstructures of $\mathrm{La_{0.333}Ca_{0.667}MnO_3}$. *Phys. Rev. B* **59**, 14440–14450 (1999).
8. Pissas, M., Margiolaki, I., Prassides, K. & Suard, E. Crystal and magnetic structural study of the $\mathrm{La_{1-x}Ca_xMnO_3}$ compound ($x = 3/4$). *Phys. Rev. B* **72**, 064426 (2005).
9. Martinelli, A., Ferretti, M. & Ritter, C. Phase separation, orbital ordering and magnetism in $(\mathrm{La_{0.375}Ca_{0.625}})\mathrm{MnO_3}$. *J. Solid State Chem.* **239**, 99–105 (2016).
10. Pissas, M., Kallias, G., Hofmann, M. & Többens, D. M. Crystal and magnetic structure of the $\mathrm{La_{1-x}Ca_xMnO_3}$ compound ($x = 0.8, 0.85$). *Phys. Rev. B* **65**, 064413 (2002).
11. Endo, T., Goto, T., Inoue, Y. & Koyama, Y. Disordered Jahn-Teller-polaron states in the simple perovskite manganite $\mathrm{Ca_{1-x}La_xMnO_3}$ with $0.15 \le x \le 0.28$. *J. Phys. Soc. Jpn.* **88**, 074708 (2019).
12. Daoud-Aladine, A., Rodríguez-Carvajal, J., Pinsard-Gaudart, L., Fernández-Díaz, M. T. & Revcolevschi, A. Zener polaron ordering in half-doped manganites. *Phys. Rev. Lett.* **89**, 097205 (2002).
13. Herrero-Martín, J., García, J., Subías, G., Blasco, J. & Sánchez, M. C. Structural origin of dipole x-ray resonant scattering in the low-temperature phase of $\mathrm{Nd_{0.5}Sr_{0.5}MnO_3}$. *Phys. Rev. B* **70**, 024408 (2004).
14. Rodriguez, E. E., Proffen, T., Llobet, A., Rhyne, J. J. & Mitchell, J. F. Neutron diffraction study of average and local structure in $\mathrm{La_{0.5}Ca_{0.5}MnO_3}$. *Phys. Rev. B* **71**, 104430 (2005).
15. García, J., Sánchez, M. C., Subías, G. & Blasco, J. High resolution X-ray absorption near edge structure at the Mn K edge of manganites. *J. Phys. Condens. Matter* **13**, 3229–3241 (2001).
16. Loudon, J. C. et al. Weak charge-lattice coupling requires reinterpretation of stripes of charge order in $\mathrm{La_{1-x}Ca_xMnO_3}$. *Phys. Rev. Lett.* **94**, 097202 (2005).
17. Mori, S., Chen, C. H. & Cheong, S.-W. Pairing of charge-ordered stripes in $(\mathrm{La,Ca})\mathrm{MnO_3}$. *Nature* **392**, 473 (1998).
18. Tao, J. & Zuo, J. M. Nanoscale phase competition during charge ordering in intrinsically strained $\mathrm{La_{0.33}Ca_{0.67}MnO_3}$. *Phys. Rev. B* **69**, 180404 (2004).
19. Tao, J., Niebieskikwiat, D., Salamon, M. B. & Zuo, J. M. Lamellar phase separation and dynamic competition in $\mathrm{La_{0.23}Ca_{0.77}MnO_3}$. *Phys. Rev. Lett.* **94**, 147206 (2005).
20. Rodríguez-Carvajal, J. Recent advances in magnetic structure determination by neutron powder diffraction. *Phys. B Condens. Matter* **192**, 55–69 (1993). Recent Developments of the Program FULLPROF, in Commission on Powder Diffraction (IUCr). Newsletter (2001), 26, 12–19. http://journals.iucr.org/iucr-top/comm/cpd/Newsletters/. The complete documentation can be obtained at http://www.ill.eu/sites/fullprof/.
21. Stephens, P. W. Phenomenological model of anisotropic peak broadening in powder diffraction. *J. Appl. Crystallogr.* **32**, 281–289 (1999).
22. Llobet, A., Frontera, C., García-Muñoz, J. L., Ritter, C. & Aranda, M. A. G. Chemical heterogeneity in a single phase: $\mathrm{Bi_{0.15}Ca_{0.85}MnO_3}$, a case example of macroscopic phase segregation. *Chem. Mater.* **12**, 3648–3657 (2000).
23. Wang, R., Gui, J., Zhu, Y. & Moodenbaugh, A. R. Distinguishing between the bi-stripe and wigner-crystal model: a crystallographic study of charge-ordered $\mathrm{La_{0.33}Ca_{0.67}MnO_3}$. *Phys. Rev. B* **61**, 11946–11955 (2000).
24. Wang, R., Gui, J., Zhu, Y. & Moodenbaugh, A. R. Crystallographic analysis of orientational domain variants and charge-ordered domains in $\mathrm{La_{0.33}Ca_{0.67}MnO_3}$. *Phys. Rev. B* **63**, 144106 (2001).
25. Pissas, M., Stamopoulos, D., Arulraj, A. & Prassides, K. Evolution of the magnetic structure in overdoped antiferromagnetic $\mathrm{La_{1-x}Ca_xMnO_3}$, $(0.51 \le x \le 0.69)$ manganites: a neutron diffraction study. *Phys. Rev. B* **107**, 035110 (2023).
26. Pissas, M. & Kallias, G. Phase diagram of the $\mathrm{La_{1-x}Ca_xMnO_3}$ compound ($0.5 < x < 0.9$). *Phys. Rev. B* **68**, 134414 (2003).
27. Milward, G. C., Calderón, M. J. & Littlewood, P. B. Electronically soft phases in manganites. *Nature* **433**, 607 (2005).
28. Zheng, R. K. et al. Transport, magnetic, specific heat, internal friction, and shear modulus in the charge ordered $\mathrm{La_{0.25}Ca_{0.75}MnO_3}$ manganite. *J. Appl. Phys.* **94**, 514–518 (2003).
29. Calvani, P. et al. Infrared absorption from charge density waves in magnetic manganites. *Phys. Rev. Lett.* **81**, 4504–4507 (1998).
30. Kim, K. H., Lee, S., Noh, T. W. & Cheong, S.-W. Charge ordering fluctuation and optical pseudogap $\mathrm{La_{1-x}Ca_xMnO_3}$. *Phys. Rev. Lett.* **88**, 167204 (2002).
31. Litvinchuk, A., Iliev, M., Pissas, M. & Chu, C. Charge and lattice dynamics of ordered state in $\mathrm{La_{1/2}Ca_{1/2}MnO_3}$: infrared reflection spectroscopy study. *Solid State Commun.* **132**, 309 – 313 (2004).
32. Cox, S. et al. Evidence for the charge-density-wave nature of the stripe phase in manganites. *J. Phys. Condens. Matter* **19**, 192201 (2007).
33. Cox, S., Singleton, J., McDonald, R. D., Migliori, A. & Littlewood, P. B. Sliding charge-density wave in manganites. *Nat. Mater.* **7**, 25 (2008).
34. Nucara, A. et al. Observation of charge-density-wave excitations in manganites. *Phys. Rev. Lett.* **101**, 066407 (2008).
35. Overhauser, A. W. Observability of charge-density waves by neutron diffraction. *Phys. Rev. B* **3**, 3173–3182 (1971).
36. Grüner, G. The dynamics of charge-density waves. *Rev. Mod. Phys.* **60**, 1129–1181 (1988).
37. Peierls, R. E. *Quantum Theory of Solids* (Oxford University, 1964).
38. Pouget, J.-P. The Peierls instability and charge density wave in one-dimensional electronic conductors. *C. R. Phys.* **17**, 332–356 (2016).
39. Fedders, P. A. & Martin, P. C. Itinerant antiferromagnetism. *Phys. Rev.* **143**, 245–259 (1966).
40. Gorshunov, B. et al. Boson peak in overdoped manganites $\mathrm{La_{1-x}Ca_xMnO_3}$. *Phys. Rev. B* **87**, 245124 (2013).
41. Zhukova, E. et al. Origin of low-energy excitations in charge-ordered manganites. *EPL* **90**, 17005 (2010).
42. Zhang, T. et al. Terahertz spectroscopy of low-energy excitations in charge-ordered $\mathrm{La_{0.25}Ca_{0.75}MnO_3}$. *Phys. Rev. B* **81**, 125132 (2010).
43. Gorshunov, B. P. et al. Nature of the low-energy excitations of a charge-ordered phase of $\mathrm{La_{0.25}Ca_{0.75}MnO_3}$ manganites. *JETP Lett.* **91**, 336–340 (2010).
44. Tao, J. et al. Direct observation of electronic-liquid-crystal phase transitions and their microscopic origin in $\mathrm{La_{1/3}Ca_{2/3}MnO_3}$. *Sci. Rep.* **6**, 37624 (2016).
45. El Baggari, I. et al. Nature and evolution of incommensurate charge order in manganites visualized with cryogenic scanning transmission electron microscopy. *Proc. Natl Acad. Sci. USA* **115**, 1445–1450 (2018).
46. Savitzky, B. H. et al. Bending and breaking of stripes in a charge ordered manganite. *Nat. Commun.* **8**, 1883 (2017).
47. Tao, J., Sun, K., Tranquada, J. M. & Zhu, Y. Anomalous nanoclusters, anisotropy, and electronic nematicity in the doped manganite $\mathrm{La_{1/3}Ca_{2/3}MnO_3}$. *Phys. Rev. B* **95**, 235113 (2017).
48. Chen, W.-T. et al. Striping of orbital-order with charge-disorder in optimally doped manganites. *Nat. Commun.* **12**, 6319 (2021).

Acknowledgements

We thank the ESRF for the provision of beamtime. This work was financially supported by Grants-in-Aid for Scientific Research (JSPS KAKENHI Grant Numbers JP18K18724, JP19H04590, JP21H01907, and JP22K18693), the Murata Science Foundation, and the Izumi Science and Technology Foundation.

Author contributions

All authors contibuted equally.

Competing interests

The authors declare no competing interests.

Additional information

Supplementary information The online version contains supplementary material available at https://doi.org/10.1038/s42005-023-01304-y.

Correspondence and requests for materials should be addressed to Michael Pissas or Kosmas Prassides.

Peer review information *Communications Physics* thanks Anna Llobet and the other anonymous reviewers for their contribution to the peer review of this work.

Reprints and permission information is available at http://www.nature.com/reprints

Publisher's note Springer Nature remains neutral with regard to jurisdictional claims in published maps and institutional affiliations.

Open Access This article is licensed under a Creative Commons Attribution 4.0 International License, which permits use, sharing, adaptation, distribution and reproduction in any medium or format, as long as you give appropriate credit to the original author(s) and the source, provide a link to the Creative Commons license, and indicate if changes were made. The images or other third party material in this article are included in the article's Creative Commons license, unless indicated otherwise in a credit line to the material. If material is not included in the article's Creative Commons license and your intended use is not permitted by statutory regulation or exceeds the permitted use, you will need to obtain permission directly from the copyright holder. To view a copy of this license, visit http://creativecommons.org/licenses/by/4.0/.

© The Author(s) 2023